COMPUTER-AIDED CIVIL AND INFRASTRUCTURE ENGINEERING

Computer-Aided Civil and Infrastructure Engineering **0** (2015) 1–11

Particle–Fluid–Structure Interaction for Debris Flow Impact on Flexible Barriers

Alessandro Leonardi, Falk K. Wittel*, Miller Mendoza, Roman Vetter & Hans J. Herrmann

Institute for Building Materials, ETH Zurich, Stefano-Franscini-Platz 3, CH-8093 Zurich, Switzerland

Abstract: *Flexible barriers are increasingly used for the protection from debris flow in mountainous terrain due to their low cost and environmental impact. However, the development of a numerical tool for the rational design of such structures is still a challenge. In this work, a hybrid computational framework is presented, using a total Lagrangian formulation of the finite element method to represent a flexible barrier. The actions exerted on the structure by a debris flow are obtained from simultaneous simulations of the flow of a fluid-grain mixture, using two conveniently coupled solvers: the discrete element method governs the motion of the grains, while the free-surface non-Newtonian fluid phase is solved using the lattice Boltzmann method. Simulations on realistic geometries show the dependence of the momentum transfer on the barrier on the composition of the debris flow, challenging typical assumptions made during the design process today. In particular, we demonstrate that both grains and fluid contribute in a nonnegligible way to the momentum transfer. Moreover, we show how the flexibility of the barrier reduces its vulnerability to structural collapse, and how the stress is distributed on its fabric, highlighting potential weak points.*

1 INTRODUCTION

Debris flows are among the most hazardous natural events, among other reasons due to their destructive potential, their unpredictability, and the difficulties in designing effective countermeasures (Iverson, 1997; Hungr and Jakob, 2005). The development of hazard maps has contributed to reduce the risk in many mountainous areas, forbidding or limiting constructions in potentially dangerous areas (van Westen et al., 2005). Often, these regulatory measures fail to reduce the risk to an acceptable level, especially for settlements already located in hazardous terrain or in situations where an unexpected event suddenly highlights a potential risk (Wendeler et al., 2012). In these cases, structural countermeasures, such as barriers, piles, check dams (Armanini et al., 1991), and detention basins, are commonly employed to further reduce the risk. A rather new countermeasure is represented by flexible barriers, which are efficiently used for quick interventions and for small basins. Structurally similar to the barriers used for snow avalanches and rockfall prevention (Volkwein et al., 2009; von Boetticher et al., 2011), they often consist of one or more steel cable nets, spanning the whole width of the riverbed while being anchored to the channel banks. The advantages of flexible barriers over rigid ones are a drastic reduction in construction costs, as well as a smaller environmental impact. They make optimal use of material and land and are easier to dismantle and substitute (Wendeler, 2008).

For an efficient design, the impact pressure exerted from the debris flow on the barrier is of utter importance. However, acquiring reliable estimates is a challenging design issue. The hydrodynamic force transmitted by the flow to the structure mainly depends on the volume of the debris material, the thickness of the incoming flow, the composition of the sediments, and on the impact speed of the flowing mass (Armanini, 1990; Bugnion et al., 2011; Canelli et al., 2012; Brighenti et al., 2013). Although this is true for any retention measure, flexible cable nets have the additional complication of being permeable to the fluid phase and to sediments smaller than the mesh size (Takahashi, 2007). The presence of a grain-size distribution in the flowing sediments, however, implies that grains larger than the mesh spacing are impounded by the net, which, in turn,

*To whom correspondence should be addressed. E-mail: *fwittel@ethz.ch*.

DOI: 10.1111/mice.12165

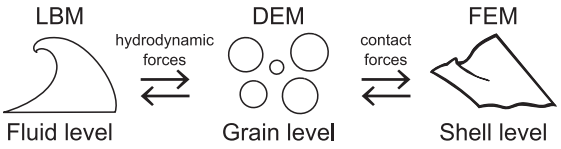

Fig. 1. Outline of the coupling scheme.

reduces permeability to smaller sized portions. When the barrier is completely clogged, even the fluid can be prevented from passing through. Due to this feedback mechanism, the peak pressure can be shifted beyond the initial impact, and the dynamic load gets distributed over a longer time period. Moreover, the flexibility of the barrier provides another means of reducing the impact momentum, because the structure adapts to the received impulse. Therefore, the assumption at the base of protection structure design, namely, the possibility of uncoupling the fluid and the structural problem, becomes incorrect.

Flexible structures are relatively new compared to rigid ones and therefore lack a comprehensive set of experimental data to aid the rational design. Full-size experiments such as the ones carried out by Volkwein et al. (2006) are extremely expensive and therefore mainly appear in single realizations. On the other hand, downscaled experiments unfortunately face the problem of scaling the various physical phenomena involved (Scheidl et al., 2012, and references therein). The motivation for this work lies in providing a numerical approach, complete and at the same time efficient, to be used for the optimization of barrier design. A similar framework has been developed by von Boetticher (2013), where the debris flow is described as a single-phase medium. We represent debris flow as a mixture of a granular and a non-Newtonian fluid phase. The grain dynamics is solved with the fluid by the lattice Boltzmann method (LBM) (Section 2.1) and the discrete element method (DEM) (Section 2.2). An outline of the coupling algorithm is given in Section 3.1. The flexible barrier is modeled using the finite element method (FEM) (Section 2.3). It only interacts with the grains and not with the fluid (see Section 3.2 for the coupling between the grains and the structure). This reduces the computational cost and at the same time it mimics the real filter features of a cable net. When grains collide with the barrier, they also transmit the hydrodynamic force, see Figure 1. An example of the scenario that this method is able to reproduce is shown in Figure 2. This setting simplifies the complexity of a debris flow but is also able to deliver a realistic simulation of the interaction between flow and obstacle.

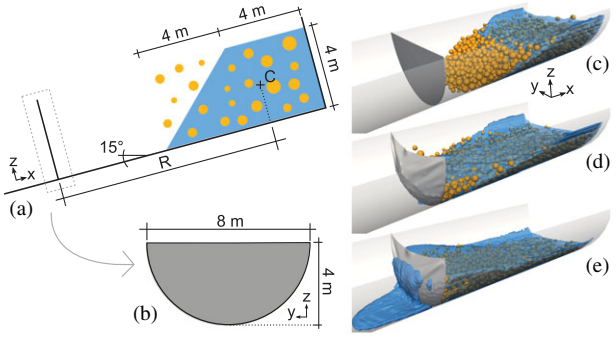

Fig. 2. The setup of our simulation. (a) Geometry of the configuration before the simulation starts. Point C is the debris center of mass. (b) Undeformed shape of the barrier. The snapshots on the right show the geometry of the flow before (c), during (d), and after (e) the impact on the barrier.

2 NUMERICAL METHODS

2.1 Debris flow continuum phase: the LBM

The simulation of debris flow is commonly performed by the use of a continuum fluid approach, often using a non-Newtonian rheology (Hutter et al., 1996; Iverson, 2003) or using two-phase mixture theories that take into account the spatial distribution of the grains (Kowalski, 2008; Kowalski and McElwaine, 2013). Alternatively, debris flow is represented by a collection of grains, tracking the individual motion of each grain (Teufelsbauer et al., 2009). Recently, efforts have been devoted to try to integrate these two approaches by describing the debris materials as a mixture of fluid and grains (Sun et al., 2013; Leonardi et al., 2013). The resulting numerical tool requires a continuum and a discrete solver. Although still not frequently employed in geophysics, this approach was successfully applied for the simulation of other similar complex fluids, such as food or concrete (Švec et al., 2012). The method we use is similar to the one described by Leonardi et al. (2014a) and is therefore only briefly outlined here, starting from the fluid solver.

The LBM is a relatively recent approach to fluid dynamics where in contrast to finite volume methods, conservation laws are not enforced on a continuum velocity and pressure field. Instead, the flowing mass is discretized as a collection of small colliding particles, represented by a probability distribution function f, which mimics the actual behavior of the fluid. The solution is made possible by a drastic reduction in the number of degrees of freedom, because the particles are only allowed to move on a fixed, regular grid, and with a velocity chosen among a discrete set $\boldsymbol{c}_i$. However, since mass and momentum conservation are

nevertheless imposed, the outcome of an LBM simulation can be proven to be equivalent to a solution of the Navier–Stokes equations. The fluid mass density ρ_f, pressure p_f, and velocity $\boldsymbol{u}_\mathrm{f}$ can be reconstructed starting from the discretized form of the distribution function f_i, as

$$\rho_\mathrm{f} = \sum_i f_i, \quad p_\mathrm{f} = c_\mathrm{s}^2 \rho_\mathrm{f}, \; \boldsymbol{u}_\mathrm{f} = \tfrac{1}{\rho_\mathrm{f}} \sum_i f_i \boldsymbol{c}_i \tag{1}$$

where c_s is the speed of sound of the lattice and the displayed sums run over the set of directions i. The dynamics of the system are governed by the lattice Boltzmann equation that, assuming a temporal and spatial discretization with unit spacing, reads

$$f_i(\boldsymbol{x}+c_i, t+1) = f_i(\boldsymbol{x}, t) + \Omega_i(\boldsymbol{x}, t) + F_i(\boldsymbol{x}, t, \boldsymbol{F}) \tag{2}$$

where Ω_i is the operator reconstructing the effect of molecular collisions. We express it using the Bhatnagar–Gross–Krook linear approximation (Bhatnagar et al., 1954), which drags the system toward the thermodynamic equilibrium state f_i^eq,

$$\Omega_i = \frac{f_i^\mathrm{eq} - f_i}{\tau} \tag{3}$$

The relaxation time τ governs the viscous behavior, being related to the viscosity of the fluid μ through

$$\tau = \frac{1}{2} + \frac{\mu(\dot{\gamma})}{c_\mathrm{s}^2} \tag{4}$$

To implement a non-Newtonian fluid, μ is set to be a function of the shear rate $\dot{\gamma}$, following the approach by Boyd et al. (2006) and Švec et al. (2012). Section 4 contains more details about the employed constitutive law (see Equation 25). The operator $F_i(\boldsymbol{x}, t, \boldsymbol{F})$ in Equation (2) implements the effects of external forcing terms $\boldsymbol{F}$ (see Section 3.1 for details).

2.2 Debris flow granular phase: the DEM

The DEM is integrated with the LBM to obtain a hybrid representation of a debris flow, both as a continuum and as a discrete medium. Particles in a debris flow have different roles based on their size. Small particles can be considered a constituent part of the fluid phase, while large particles develop the typical phenomena of granular matter, such as segregation and the formation of levees, granular fronts, and shock waves (Iverson, 2003). Following this classification, only a portion of the particles is simulated, with the intent of representing effects due to large grain dynamics (Leonardi et al., 2013). In addition, particles are assumed to have a spherical shape for simplicity. The motion of every grain is calculated by solving Newton's equations of motion for translational and rotational degrees of freedom in a fashion that has become standard for DEM simulations (Pöschel and Schwager, 2005; Bićanić, 2007). Whenever two grains come into contact, a repulsive force $\boldsymbol{F}_\mathrm{coll}$ is applied as a function of the overlap between the two grains

$$\xi = r_1 + r_2 - ||\boldsymbol{d}_{1,2}|| \tag{5}$$

where $\boldsymbol{d}_{1,2}$ denotes the distance vector between the center points of the grains, and r_1 and r_2 are their respective radii. The normal repulsive forces are calculated according to the Hertzian theory of viscoelastic collisions as

$$F_\mathrm{coll}^\mathrm{n} = \frac{2}{3} \frac{E_\mathrm{g} \sqrt{r_\mathrm{eff}}}{\left(1 - \nu_\mathrm{g}^2\right)} \left(\xi^{3/2} + A \sqrt{\xi} \frac{d\xi}{dt} \right) \tag{6}$$

with the Young's modulus E_g and Poisson's ratio ν_g^2 of the grains, while A represents the damping constant (Brilliantov et al., 1996), and r_eff is the effective radius defined as $r_\mathrm{eff} = r_1 r_2 \, (r_1 + r_2)$. Two grains in contact exchange also tangential forces, proportional to their relative tangential velocity $u_\mathrm{rel}^\mathrm{t}$ and limited by Coulomb's friction law as

$$F_{coll}^{\mathbf{t}} = -\mathrm{sign}\left(u_{rel}^t\right) \min\left\{ \gamma \left| u_{rel}^t \right|, \tan(\psi) \, F_{coll}^n \right\} \tag{7}$$

where ψ is the dynamic friction angle and γ is the shear damping coefficient.

Analogous principles are used for the solution of contacts with rigid walls or flexible obstacles. The forces arising from the collisions are added to the hydrodynamic interaction coming from the LBM, and to the gravitational force. The dynamics of the system are finally solved using a Gear predictor–corrector scheme (Gear, 1971).

2.3 Thin shell with large deformations: the subdivision surfaces FEM

The flexible barrier is represented by an FEM discretization of a thin shell in a total Lagrangian formulation. The method is only briefly outlined here and for further details, we refer to Vetter et al. (2013) and references therein.

The underlying constitutive model follows the Kirchhoff–Love theory of thin shells, which is valid for shell thicknesses h_s much smaller than the in-plane shell dimensions. The middle surface of the shell is parameterized in both its stress-free reference ($\overline{\Omega}$) and deformed (Ω) configuration. The indices $i, j, k, l = 1, 2$ denote covariant (subscripts) or contravariant (superscripts) components of vectors and tensors. Let $\{\theta^1, \theta^2, \theta^3\}$ be a convected curvilinear coordinate system with θ^1, θ^2 spanning the middle surface and θ^3 orthogonal to it. Any point on the middle surface can then be written as $\overline{\boldsymbol{x}}(\theta^1, \theta^2) \in \bar{\Omega}$ when referring to the undeformed surface, and as $\boldsymbol{x}(\theta^1, \theta^2) \in \Omega$ when

referring to the deformed surface. The position of arbitrary material points within the shell follows the same principles and is written as

$$\begin{aligned}\overline{\boldsymbol{p}}(\theta^1,\theta^2,\theta^3) &= \overline{\boldsymbol{x}}(\theta^1,\theta^2) + \theta^3\,\overline{\boldsymbol{a}}_3(\theta^1,\theta^2)\\ \boldsymbol{p}(\theta^1,\theta^2,\theta^3) &= \boldsymbol{x}(\theta^1,\theta^2) + \theta^3\boldsymbol{a}_3(\theta^1,\theta^2)\end{aligned} \tag{8}$$

The terms $\bar{\boldsymbol{a}}_3$ and $\boldsymbol{a}_3$ are local directors for the surfaces $\bar{\Omega}$ and Ω. The first two components are tangent to the surface, and are obtained through differentiation as

$$\overline{\boldsymbol{a}}_i(\theta^1,\theta^2) = \frac{\partial\bar{\boldsymbol{x}}}{\partial\theta^i},\ \boldsymbol{a}_i(\theta^1,\theta^2) = \frac{\partial\boldsymbol{x}}{\partial\theta^i} \tag{9}$$

The third component is computed according to the Kirchhoff hypotheses that straight material lines that are normal to the middle surface retain their straightness, normality, and length in any deformed configuration; thus:

$$\bar{\boldsymbol{a}}_3 = \frac{\bar{\boldsymbol{a}}_1\times\bar{\boldsymbol{a}}_2}{||\bar{\boldsymbol{a}}_1\times\bar{\boldsymbol{a}}_2||},\ \boldsymbol{a}_3 = \frac{\boldsymbol{a}_1\times\boldsymbol{a}_2}{||\boldsymbol{a}_1\times\boldsymbol{a}_2||} \tag{10}$$

With this formulation, strain measures can be expressed in a convenient form. We can obtain the covariant components of the first fundamental form as

$$\bar{a}_{ij} = \bar{\boldsymbol{a}}_i\cdot\bar{\boldsymbol{a}}_j,\ a_{ij} = \boldsymbol{a}_i\cdot\boldsymbol{a}_j \tag{11}$$

and those of the second fundamental form as

$$\bar{b}_{ij} = \bar{\boldsymbol{a}}_3\cdot\frac{\partial\bar{\boldsymbol{a}}_i}{\partial\theta^j},\ b_{ij} = \boldsymbol{a}_3\cdot\frac{\partial\boldsymbol{a}_i}{\partial\theta^j} \tag{12}$$

The in-plane (2×2) membrane and bending strain tensors in curvilinear coordinates then derive from the fundamental forms as

$$\alpha_{ij} = \tfrac{1}{2}\left(a_{ij}-\bar{a}_{ij}\right),\ \beta_{ij} = \bar{b}_{ij}-b_{ij} \tag{13}$$

Although the total Lagrangian formulation correctly represents the geometrical nonlinearity due to the large displacements, a complete model should also take into account the material nonlinearity of the steel cable net. As a first approximation, we assume that the shell material is linearly elastic, and therefore characterized only by a Young's modulus E_s and a Poisson's ratio ν_s. The shell total elastic energy is then given by the integral of the Koiter energy density functional over the middle surface (van der Heijden, 2008)

$$\begin{aligned}U_\mathrm{e}\ [\bar{\boldsymbol{x}},\boldsymbol{x}] = \frac{1}{2}\int_{\bar{\Omega}} & h_\mathrm{s}\,\alpha_{ij}C^{ijkl}\alpha_{kl}\\ &+\frac{h_\mathrm{s}^3}{12}\beta_{ij}C^{ijkl}\beta_{kl}\mathrm{d}\bar{\Omega}\end{aligned} \tag{14}$$

where $\mathrm{d}\bar{\Omega} = ||\bar{\mathrm{a}}_1\times\ \bar{\mathrm{a}}_2||\ \mathrm{d}\theta^1\mathrm{d}\theta^2$. The elastic tensor is given componentwise by

$$C^{ijkl} = \frac{E_\mathrm{s}}{1-\nu_\mathrm{s}^2}\left(\nu_\mathrm{s}\,\bar{a}^{ij}\,\bar{a}^{kl} + \frac{1-\nu_\mathrm{s}}{2}\left(\bar{a}^{ik}\,\bar{a}^{jl}+\bar{a}^{il}\,\bar{a}^{jk}\right)\right) \tag{15}$$

in curvilinear coordinates. Inertial forces are included by adding a kinetic energy contribution of the form

$$U_\mathrm{k}[\boldsymbol{x}] = \frac{1}{2}\int_{\bar{\Omega}} h_\mathrm{s}\rho_\mathrm{s}\dot{\boldsymbol{x}}\cdot\dot{\boldsymbol{x}}\mathrm{d}\bar{\Omega} \tag{16}$$

where ρ_s is the shell mass density and $\dot{\boldsymbol{x}} = \frac{\partial\boldsymbol{x}}{\partial t}$ is the velocity.

The total energy $U = U_\mathrm{e} + U_\mathrm{k}$ is minimized with the FEM in weak formulation. To allow for a mathematically sound representation of the bending field, the shape functions need to be differentiable with continuous derivatives (class C^1) over the whole domain. We satisfy this requirement by adopting the subdivision surface paradigm (Cirak et al., 2000; Cirak and Ortiz, 2001). The use of subdivision surface shape functions avoids the introduction of auxiliary degrees of freedom such as rotations and is therefore particularly efficient. The dynamic problem is solved through time integration with a predictor–corrector scheme from the Newmark family (Newmark, 1959).

3 COUPLING SCHEMES FOR THE HYBRID APPROACH

3.1 Debris flow as hybrid media: the LBM—DEM coupling

Grains interact with the fluid through a forcing term acting on the LBM velocity field. To achieve this, we employ a simplified version of the immersed boundary method (Owen et al., 2011) that has the basic assumption that the fluid fills the entire domain, including the interior of the grains. Although the fluid located inside the particles is not considered part of the flowing mass, it is nevertheless solved and its properties are used to compute the hydrodynamic interaction forces. Fluid elements located away from the grains are not directly influenced by the coupling. All nodes located inside of a grain, on the other hand, are subjected to a forcing term $\boldsymbol{p}$ that relaxes the velocity of the fluid to the velocity of the grain. This is included together with gravity $\boldsymbol{g}$ in Equation (2) inside the forcing term $\boldsymbol{F} = \boldsymbol{p} + \boldsymbol{g}$. For all nodes located outside of grains, this reduces to $\boldsymbol{F} = \boldsymbol{g}$. If $\boldsymbol{x}$ is the location of the fluid node, $\boldsymbol{p}$ can be computed, assuming the unit volume of a lattice node, as

$$\boldsymbol{p}(\boldsymbol{x},t) = \rho_\mathrm{f}(\boldsymbol{x},t)\left[\boldsymbol{u}_\mathrm{f}(\boldsymbol{x},t) - \boldsymbol{u}_\mathrm{g}(\boldsymbol{x},t)\right] \tag{17}$$

where $\boldsymbol{u}_{\mathrm{f}}(\boldsymbol{x}, t)$ denotes the velocity of the fluid and $\boldsymbol{u}_{\mathrm{g}}(\boldsymbol{x}, t)$ is the velocity of the grain at the same position. Since grains are rigid bodies, $\boldsymbol{u}_{\mathrm{g}}(\boldsymbol{x}, t)$ can be calculated as

$$\boldsymbol{u}_{\mathrm{g}}(\boldsymbol{x}, t) = \boldsymbol{u}_{\mathrm{g}}(\boldsymbol{x}_{\mathrm{c}}, t) + (\boldsymbol{x} - \boldsymbol{x}_c) \times \boldsymbol{\omega}_{\mathrm{g}} \tag{18}$$

where $\boldsymbol{u}_{\mathrm{g}}(\boldsymbol{x}_{\mathrm{c}}, t)$ and $\boldsymbol{\omega}_{\mathrm{g}}$ are the translational and rotational velocities of the grain, respectively, and $\boldsymbol{x}_{\mathrm{c}}$ is the position of its center of mass. To improve the stability of this scheme, the viscosity of the fluid lying inside the grain is set to a high value.

The forcing term $\boldsymbol{F}$ is determined, following the approach of Guo et al. (2002), through the addition of the extra term $F_i\ (\boldsymbol{x}, t, \boldsymbol{F})$ in Equation (2), and modifying the computation of the velocity field in Equation (1) with

$$\boldsymbol{u}_{\mathrm{f}} = \frac{1}{\rho_{\mathrm{f}}} \left(\sum_i f_i \boldsymbol{c}_i + \frac{\boldsymbol{F}}{2} \right) \tag{19}$$

The same force with an opposite sign is applied to the grains. The overall force $\boldsymbol{F}_{\mathrm{grain}}$ and torque $\boldsymbol{T}_{\mathrm{grain}}$ acting on an element is therefore the sum of all contributions from the nodes j lying inside the grain itself:

$$\begin{aligned} \boldsymbol{F}_{\mathrm{grain}} &= -\sum_j \boldsymbol{p}_j\,(\boldsymbol{x}_j) \\ \boldsymbol{T}_{\mathrm{grain}} &= -\sum_j \boldsymbol{p}_j\,(\boldsymbol{x}_j) \times\ (\boldsymbol{x}_j - \boldsymbol{x}_c) \end{aligned} \tag{20}$$

This is transmitted to the DEM solver and is added up to the collection of forces for the equations of motion.

3.2 The shell as flexible barrier: the DEM–FEM coupling

When a grain collides with the shell, a repulsive force is exerted on both elements, following an approach similar to the grain-to-grain contact of Section 2.2. For this purpose, a set of points is generated from the deformed state of the shell $\bar{\boldsymbol{x}}$, and is used for the resolution of contacts. This approach mimics the actual behavior of a cable-net barrier, because grains smaller than the point spacing are allowed to pass through.

The overlap between a grain g of radius r_{g} and a shell point p is calculated in a similar way to the grain–grain overlap:

$$\xi = r_g - ||\boldsymbol{d}_{\mathrm{p,g}}|| \tag{21}$$

where $\boldsymbol{d}_{\mathrm{p,g}}$ denotes the distance vector between the center of the grain and the shell point. When positive, this overlap is used to calculate a normal repulsion force $\boldsymbol{F}^{\mathrm{n}}_{\mathrm{obstacle}}$ using Equation (6).

The treatment of the tangential force differs significantly from the particle–particle contact model. Here, to model the trapping effect of the barrier, the tangential viscous force is substituted with a static Coulomb friction component. This is added through an elastic spring introduced in the plane orthogonal to $d_{\mathrm{p,g}}$, which is initialized at the time of initial contact with the barrier t_{init} and is removed when a limit elongation is reached. The elongation

$$\zeta = \int_{t_{\mathrm{init}}}^{t} u^{\mathrm{t}}_{\mathrm{rel}} \mathrm{d}t \tag{22}$$

is used to determine together with the spring stiffness k, the restoring force, as

$$F^{\mathrm{t}}_{\mathrm{obstacle}} = -\mathrm{sign}\left(u^{\mathrm{t}}_{\mathrm{rel}}\right) \min\left\{k\,|\zeta|\,, \tan(\psi)\,F^{\mathrm{n}}_{\mathrm{obstacle}}\right\} \tag{23}$$

where k is chosen in first approximation to be equal to the shell stretching stiffness

$$k = \frac{E_{\mathrm{s}} h_{\mathrm{s}}}{1 - \nu_{\mathrm{s}}^2} \tag{24}$$

The resulting force is transmitted to both the colliding DEM grain and the FEM mesh. This elastic component is essential to avoid excessive sliding of grains on the net surface, but is deemed unnecessary for the particle–particle contact model, where friction is modeled in a simpler fashion (see Equation 7).

We chose contact points to be coincident to mesh nodes. This avoids interpolations between the contact points and the mesh nodes. Since we use a regular mesh, the characteristic filtering properties of the barrier are determined by the element size. Note that this makes the contact physics dependent on the mesh resolution, which could be considered undesirable. However, in our simulations, the overall mesh size, as determined by a convergence study, is already rather fine. Our approach is motivated by simplicity and could well be refined without changes to the methodology. If higher precision is needed, the limit surface of the subdivision shell instead of the deformed control mesh can be used. This comes at the cost of longer simulation times, but allows for a higher precision (Vetter et al., 2013).

4 REFERENCE GEOMETRY OF A FLEXIBLE BARRIER MODEL

Our simulations are carried out following the geometries of *in situ* experiments, of the sort of that in Bugnion et al. (2011). We reproduce a gully riverbed of cylindrical shape with a diameter of $W = 8$ m (see Figure 2). The debris center of mass C is positioned at a variable distance R from the barrier and is instantaneously released at the beginning of the simulation, similarly to the procedure recommended for the dam-break test. The front of the flow is artificially enriched with grains

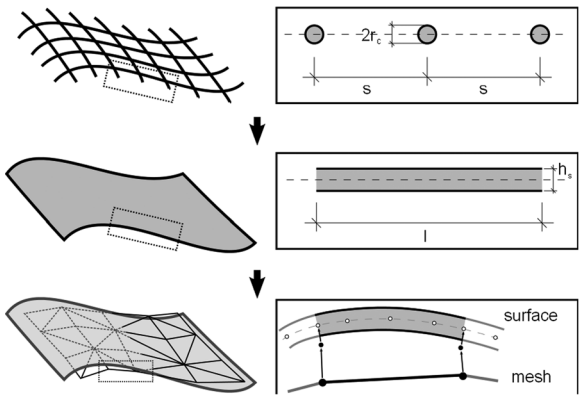

Fig. 3. The cable-net structure of the barrier is modeled with the FEM as a shell with equivalent stiffness, see Equation (26).

to resemble the observed impact conditions. The material then accelerates under the effect of gravity, which has a component both in the x direction (the longitudinal direction of the channel) and in the z direction (vertical). The ratio between the two accelerations gives the inclination of the channel, which is fixed to 15°. The channel is 22 m + R long and is loaded with 140 m^3 of fluid. The chosen non-Newtonian rheological law for the fluid is the Bingham plastic, which is the most commonly adopted when describing mudflow rheology (Kaitna et al., 2007) and can be easily implemented with the LBM (Leonardi et al., 2014b). It is defined by

$$\begin{cases} \dot{\boldsymbol{\gamma}} = 0 & \text{if fluid has not yielded } (||\boldsymbol{\sigma}|| < \sigma_y) \\ \boldsymbol{\sigma} = \sigma_y \frac{\dot{\boldsymbol{\gamma}}}{||\dot{\boldsymbol{\gamma}}||} + 2\mu_{\mathrm{pl}}\dot{\boldsymbol{\gamma}} & \text{if fluid has yielded } (||\boldsymbol{\sigma}|| > \sigma_y) \end{cases} \quad (25)$$

where $\dot{\boldsymbol{\gamma}}$ and $\boldsymbol{\sigma}$ are the shear rate and the shear stress tensor, respectively, and the vertical bars $\|\cdot\|$ denote their magnitudes (i.e., the square root of the second invariant). The scalars σ_{y} and μ_{pl} are the yield stress and the plastic viscosity. All results shown in the next section are obtained with $\sigma_{\mathrm{y}} = 500$ Pa, $\mu_{\mathrm{pl}} = 50$ Pa/s, and fluid mass density $\rho_{\mathrm{f}} = 1{,}500$ kg/m^3. The fluid phase is mixed with a variable amount of grains up to 34 m^3. The grain radii are sampled randomly from a uniform distribution between 0.1 and 0.25 m with a mass density of $\rho_{\mathrm{g}} = 2{,}500$ kg/m^3.

The actual barrier is usually a complex reticular structure, made up of diverse combinations of steel cable nets of different sizes and shapes. In this work, we consider a simplified structure, as shown in Figure 3, composed of steel cables with radius r_{c}, Young's modulus E_{c}, and regular spacing s. The barrier is modeled using shell elements, whose material and geometric characteristics need to be determined to match those of a cable net. We do so by setting the Young's modulus and the thickness of the shell to equivalent values E_{s} and h_{s}. These values are calculated by imposing that a structural element of unit length ($l = 1$) has the same stretching stiffness as the equivalent net. We obtain:

$$\pi E_{\mathrm{c}} r_{\mathrm{c}}^2 \frac{l}{s} = h_{\mathrm{s}} E_{\mathrm{s}} l \quad (26)$$

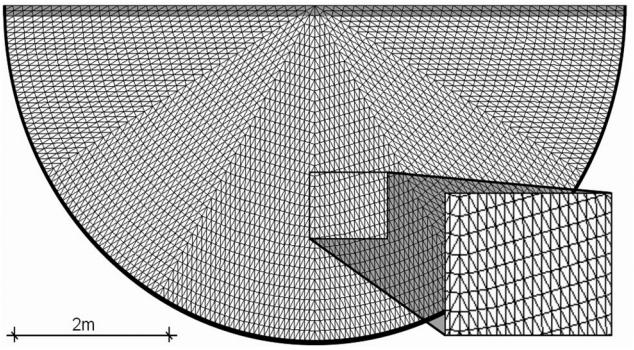

Fig. 4. Discretization of the shell mesh. The half circle is pinned along the solid black line and has a free edge at the top rim. The darker layer at the free edge has a higher stiffness.

The simulations of the next chapter aim to reproduce a barrier with $s = 0.3$ m, $r_{\mathrm{c}} = 1.1$ mm, and $E_{\mathrm{c}} = 200$ GPa. This is achieved by imposing $E_{\mathrm{s}} = 0.26$ GPa and $h_{\mathrm{s}} = 0.01$ m.

The discretization of the barrier is shown in Figure 4. Along the semicircular boundary, translation is blocked and rotation is allowed. Along the top rim, both translation and rotation are unrestricted. Actual debris flow barriers are complemented with reinforcement cables of different sizes to increase the stiffness at critical points. This is particularly important at the upper rim of the barrier to avoid excessive overspill and to improve the retention. To reproduce the same behavior without implementing further models, the upper elements of the shell are stiffened up to 10 times the value of the remainder of the barrier (see Figure 4). This additional stiffness corresponds to a single cable three times thicker than on the remainder of the net, which is realistic.

Note that linear, isotropic behavior is only a crude approximation of the reticular mechanical behavior. In principle, this can be replaced by the characteristic nonlinear, anisotropic, and plastic behavior of specific wire mesh configurations and orientations under large deformations, at the cost of a more complex formulation (see Cirak and Ortiz, 2001) and longer simulation times.

The material constants used for the simulations presented in the next section (unless differently specified) are summarized in Table 1. A typical simulation with these parameters runs with time steps of the order of 10^{-4} s for the LBM and FEM solver, and 10^{-5} s for the DEM solver. The simulation of a 20 s flow with the described geometry requires a runtime of about 20 hours

Table 1
Recap of material parameters

Material constant	*Symbol*	*Value*
Fluid plastic viscosity	μ_{pl}	50 Pa · s
Fluid yield stress	σ_y	500 Pa
Fluid density	ρ_f	1,500 kg/m^3
Grain shear damping	γ	10 kg/s
Grain normal damping	A	0.01 s
Grain friction angle	ψ	35°
Grain Young's modulus	E_g	10^8 Pa
Grain Poisson's ratio	ν_g	0.3
Grain mass density	ρ_g	2,500 kg/m^3
Grain-barrier static friction spring stiffness	k	3×10^5 N/m
Max. spring elongation	ζ_{max}	0.1 m
Shell Young's modulus	E_s	2.6×10^8 Pa
Shell Poisson's ratio	ν_s	0.33
Shell thickness	h_s	0.01 m
Shell density	ρ_s	90 kg/m^3

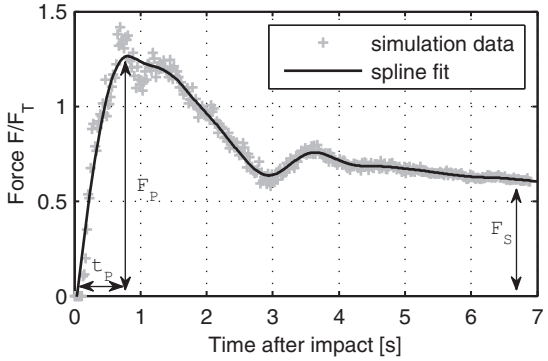

Fig. 5. Typical force evolution, depicting the total action of the debris on the net in the longitudinal direction of the channel.

on four cores with an Intel Xeon E5-1620 processor at 3.60 GHz.

5 RESULTS OF DEBRIS IMPACTS ON THE BARRIER

The principal value of interest is the force F transmitted from the flow to the barrier and specifically the component orthogonal to the deformed surface (see Figure 5). It is calculated by a sum of the FEM–DEM contact forces over all grains. The force evolution over time always presents an initial sharp increase followed by the relaxation to a stationary value.

We analyze the force evolution by fitting a spline to the numerical data, which is then differentiated to obtain the peak force F_P (corresponding to the first inflection point), the delay of the peak from the moment of initial impact t_S, and the stationary force at the tail F_S. The observed evolution is consistent with earlier experimental findings (Moriguchi et al., 2009; Chanut et al., 2010; Teufelsbauer et al., 2011; Faug et al., 2011; Caccamo et al., 2012). Due to the flexible nature of the barrier, the burst duration t_P is large compared to rigid obstacle impact. All force measures are presented in a dimensionless form, through division by the reference static load F_T in the channel longitudinal direction (with inclination of 15° with respect to the horizon), calculated as

$$F_T = m_T g \sin(15^\circ) \tag{27}$$

where m_T denotes the total mass of the debris (grains and fluid) and g the gravitational acceleration.

We study the barrier defined in the previous section. In the first simulation set, the force evolution is obtained using a variable number of grains, i.e., by varying the grain content

$$\phi = V_{grains}/V_{tot} \tag{28}$$

If both phases are present, the total volume is composed of fluid and grains $V_{tot} = V_{grains} + V_{fluid}$. If instead only grains are simulated, V_{tot} is the volume of the grains together with the volume of the empty space between them. The number of grains N_{grains} is between 100 and 1,300, and therefore ϕ is between 0.02 and 0.28. Figure 6a shows how the force evolution changes with the increase in grain content. The higher the grain content is, the quicker the barrier permeability will be reduced. For this reason, the peak value F_P in Figure 6b is increasing with ϕ. Furthermore, a quicker reduction of the barrier permeability means that the amount of material impounded by the barrier itself is increasing, leading to a growing stationary force F_S, too.

To understand the influence of the fluid phase on the force evolution, we perform two series of simulations: wet (grains with fluid) and dry (only grains, no fluid). To obtain comparable results, the forces recorded in dry simulations have been scaled by a reference static load F_T that takes into account the grain mass alone. The difference between the wet and the dry force evolutions with identical grain content is shown in Figure 7, exhibiting the resulting difference in peak and stationary forces. At high grain content, wet and dry cases show similar forces. For the wet case, this is surprising because the model does not explicitly take into account the interaction between fluid and barrier. However, a higher grain content induces a quicker saturation of the barrier, which, in turn, increases the amount of retained fluid and the recorded impulse. At low grain content, forces in the dry case are significantly higher, because

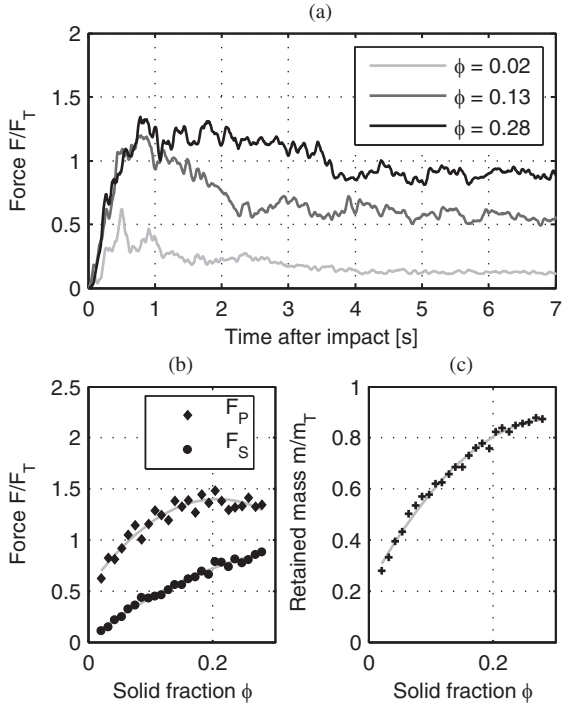

Fig. 6. Characterization of the impact force evolutions as functions of the grain content ϕ (a). Stationary and peak forces increase as the grain content becomes higher (b). Also, the retained mass increases, approaching the total mass for higher grain contents (c).

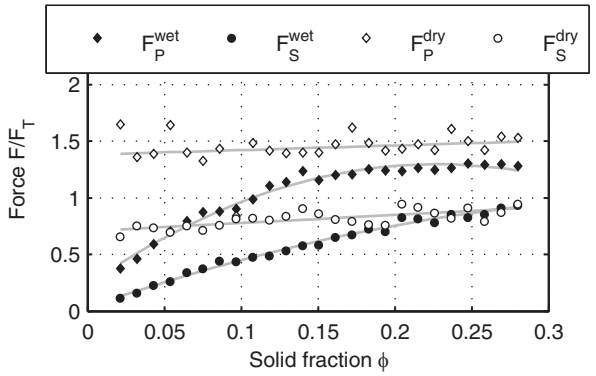

Fig. 7. Comparison between simulations with fluid (filled-in markers) and without fluid (empty markers).

the whole mass is retained by the barrier. This does not realistically represent the filtering behavior observed in real cable-net barriers, where a conspicuous part of the mass is allowed to pass through.

The bottom right panel of Figure 6 shows how the retained mass of material (both fluid and grains) increases with higher grain contents. The combination of the results in Figures 6 and 7 suggests that the design of a barrier should always be tested against a fluid debris

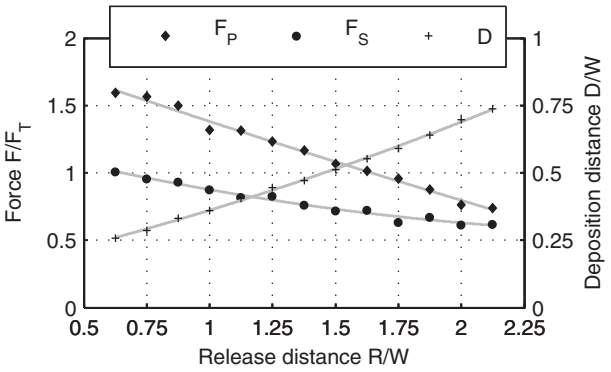

Fig. 8. Characterization of the force evolution as a function of the release distance from the barrier R. The deposition of material in the channel lowers the stationary and peak force. The final deposition distance D is also shown.

flow with high grain content. This challenges the design procedures based on the simplification of modeling the debris flow as a purely discrete or purely liquid material, which might be overconservative. We show how none of the phases should be neglected, when calculating the impact force. Because of this observation, all results presented in the following are obtained using the hybrid model with the highest particle content ($\phi = 0.28$).

The motion of the debris mass can be conceptually divided into two parts. In the first, the material accelerates, while in the second part, the flow velocity is reduced and the deposition process takes place. To study the effect of the channel length on the force evolution, we perform a set of simulations, each differing in the release distance R, between 10 and 20 m. The results (Figure 8) show how the initial peak, which can be assumed to be proportional to the dynamic load, is decreasing for larger distances. The stationary load is also decreasing, indicating that more and more material is deposited in the channel before the barrier. Figure 8 also shows the final distance of the debris center of mass from the barrier. The further away from the barrier the debris is released, the more of it is deposited in the channel before the barrier, leading to a lower force impact.

Traditional barriers are modeled as rigid obstacles, enabling the designer to consider the structural and the hydrodynamic problems separately. Most design guidelines are based on an impact force estimation that relies on this hypothesis (Hübl et al., 2009). The maximum impact force is generally calculated as a function of the dynamic load, proportional to the square of the flow velocity. In flexible barriers, this dynamic load can be consistently reduced by the flexibility of the structure. To show this, we present a set of simulations sharing the same debris configuration, and therefore the external action, but differing in the stiffness of the barrier. We

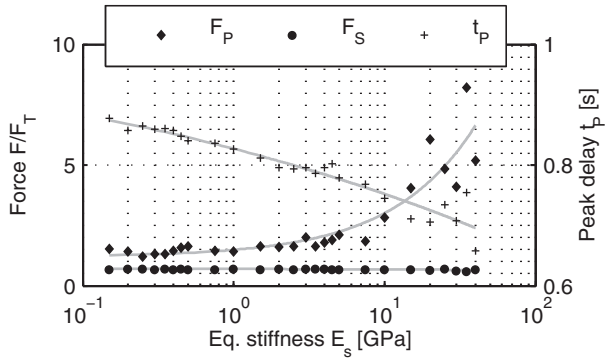

Fig. 9. Characterization of the force evolution as a function of the barrier stiffness. The peak force, related to the dynamic load, decreases for a flexible structure. A stiffer structure is subjected to a stronger and quicker initial burst.

vary the stiffness by three orders of magnitude, from a minimum shell Young's modulus E_s of 0.05 GPa to a maximum of 50 GPa (see Figure 9). This, using Equation (26), corresponds to a steel ($E_c = 200$ GPa) cable-net barrier with spacing $s = 0.3$ m and a cable radius ranging from a minimum of $r_{c,min} = 0.5$ mm to a maximum of $r_{c,max} = 15.5$ mm. This range is compatible with a wide range of configurations, comprising the one used in applications (see Wendeler, 2008).

The same debris flow transmits a much higher peak force to a stiffer structure, while the stationary force shows no dependence. The amount of impounded material is the same, but a flexible structure is safer from structural collapse. The mechanism of force reduction is revealed by Figure 9. The duration of the initial burst is longer for more flexible structures, allowing for an adsorption of the dynamic load over longer times, and therefore reducing its peak. This is, however, no general statement. The results obtained by Wendeler (2008) show that the maximum impact force is lower for rigid barriers because the flow, rather than being stopped, gets deviated in the vertical direction. In our configuration, we found this effect to be small compared to the increase in the maximum force due to the stiffer barrier. As a general result, the stiffness of the barrier should be tuned on the estimated ratio between static and dynamic load. Stiffer barriers are safer for larger and slower debris flow, while flexible barriers might be more effective in reducing the collapse risk during the impact with fast, inertial flows.

A key feature of our numerical framework is the capability to yield information about the stress distribution in the barrier. The deformed configuration of the barrier, according to the simulation with $\phi = 0.28$ and $R = 10$ m, is shown in Figure 10. The color contours indicate the elastic stretching energy per unit area of

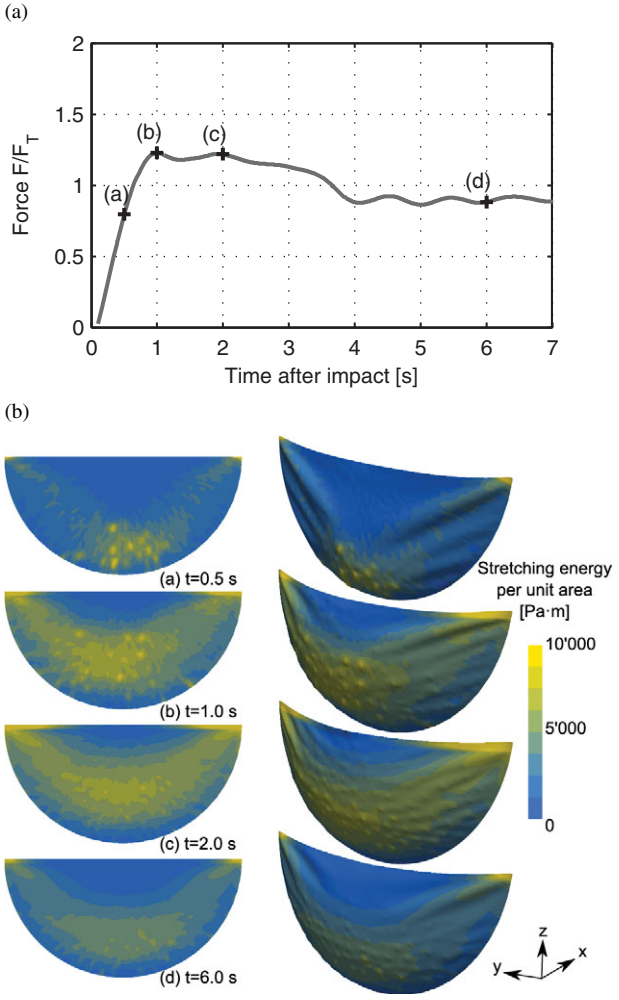

Fig. 10. Stretching energy distribution in the barrier, for $\phi = 0.28$ and $R = 10$ m. The considered time steps are indicated by the orange points in the force evolution. The pictures on the right are renderings of the deformed shell, while the pictures on the left have neither deformation nor 3D shadings for clarity.

the shell, as obtained from Equation (14). It clearly shows how the stress is localized at the upper corners of the barrier, where the shell has been stiffened. The force distribution on the supports can be inferred from this, showing how the upper supports are the ones under the highest and possibly critical load. Due to the small thickness of the shell in this example, the bending energy is negligible compared to the stretching energy.

6 SUMMARY AND OUTLOOK

A computational framework has been established, able to couple the FEM representation of a cable-net barrier with an idealized debris flow. The debris flow is obtained through a further coupling between the DEM

and the LBM, with both the granular component and the fluid explicitly represented.

The missing coupling between the fluid (LBM) and the barrier (FEM), which should be the least significant interaction due to the cable net permeability, has been neglected. Nevertheless, these two components indirectly interact through mutual coupling with the granular phase (DEM), which transmits hydrodynamic forces to the barrier. This choice is motivated by the rapid clogging of the barrier that is observed for high particle contents. We were, however, not able to numerically quantify the effect of this assumption, and leave the proof for a later work. The results show how both granular and fluid components of the debris flow have a key impact on the force evolution, challenging design assumptions based on neglecting one of the two phases. The effect of the flexibility of the structure has also been studied, showing how a flexible barrier is more efficient in reducing the peak impact force, and in distributing the dynamic load over a longer time.

Further research in this direction will focus on designing the granular phase based on field data and understanding how to calibrate the filtering properties of the barrier based on the grain characteristics and vice versa. For the same reason, the filtering properties of the barrier should be independent of the shell discretization, to leave the freedom to choose the mesh size only based on convergence criteria. Statistical fluctuations due to the variability in the flow initialization, in the properties of the materials, and in the channel geometry also need further study. Currently, we are adding material anisotropy and plasticity to the shell approach that, along with nonlinear elasticity, e.g., a Green elastic material behavior, are the main elements for representing homogenized wire mesh mechanics.

ACKNOWLEDGMENTS

The research leading to these results has received funding from the European research network MUMOLADE (Multiscale Modelling of Landslides and Debris Flow), the ETH Zurich by ETHIIRA grant no. ETH-03 10–3, as well as from the European Research Council Advanced Grant no. 319968-FlowCCS. We thank Corinna Wendeler from Geobrugg AG - Geohazard Solutions for valuable discussions.

REFERENCES

Armanini, A. (1990), On the dynamic impact of debris flows, in A. Armanini and M. Michiue (eds.), *Recent Developments on Debris Flows*, Springer, Berlin, Heidelberg, pp. 208–26.

Armanini, A., Dellagiacoma, F. & Ferrari, L. (1991), From the check dam to the development of functional check dams, in A. Armanini and G. Di Silvio (eds.), *Fluvial Hydraulics of Mountain Regions*, Springer, Berlin, Heidelberg, pp. 331–44.

Bhatnagar, P. L., Gross, E. P. & Krook, M. (1954), A model for collision processes in gases. I. Small amplitude processes in charged and neutral one-component systems, *Physical Review*, **94**(3), 511–25.

Bićanić, N. (2007), Discrete element methods, in E. Stein, R. deBorst, and T. J. R. Hughes (eds.), *Encyclopedia of Computational Mechanics*, John Wiley & Sons, Ltd., Chichester, England, pp. 311–37.

Boyd, J., Buick, J. & Green, S. (2006), A second-order accurate lattice Boltzmann non-Newtonian flow model, *Journal of Physics A: Mathematical and General*, **39**(46), 14241–47.

Brighenti, R., Segalini, A. & Ferrero, A. M. (2013), Debris flow hazard mitigation: a simplified analytical model for the design of flexible barriers, *Computers and Geotechnics*, **54**, 1–15.

Brilliantov, N., Spahn, F., Hertzsch, J. & Pöschel, T. (1996), Model for collisions in granular gases, *Physical Review E*, **53**(5), 5382–92.

Bugnion, L., McArdell, B. W., Bartelt, P. & Wendeler, C. (2011), Measurements of hillslope debris flow impact pressure on obstacles, *Landslides*, **9**(2), 179–87.

Caccamo, P., Chanut, B., Faug, T., Bellot, H. & Naaim-Bouvet, F. (2012), Small-scale tests to investigate the dynamics of finite-sized dry granular avalanches and forces on a wall-like obstacle, *Granular Matter*, **14**(5), 577–87.

Canelli, L., Ferrero, A. M., Migliazza, M. & Segalini, A. (2012), Debris flow risk mitigation by the means of rigid and flexible barriers–experimental tests and impact analysis, *Natural Hazards and Earth System Science*, **12**(5), 1693–99.

Chanut, B., Faug, T. & Naaim, M. (2010), Time-varying force from dense granular avalanches on a wall, *Physical Review E*, **82**, 041302.

Cirak, F. & Ortiz, M. (2001), Fully C1-conforming subdivision elements for finite deformation thin-shell analysis, *International Journal for Numerical Methods in Engineering*, **51**, 813–33.

Cirak, F., Ortiz, M. & Schroder, P. (2000), Subdivision surfaces: a new paradigm for thin-shell finite-element analysis, *International Journal for Numerical Methods in Engineering*, **47**, 2039–72.

Faug, T., Caccamo, P. & Chanut, B. (2011), Equation for the force experienced by a wall overflowed by a granular avalanche: experimental verification, *Physical Review E*, **84**, 051301.

Gear, C. W. (1971), The automatic integration of ordinary differential equations, *Communications of the ACM*, **14**(3), 176–79.

Guo, Z., Zheng, C. & Shi, B. (2002), Discrete lattice effects on the forcing term in the lattice Boltzmann method, *Physical Review E*, **65**, 046308.

Hübl, J., Suda, J., Proske, D., Kaitna, R. & Scheidl, C. (2009), Debris flow impact estimation, in *Proceedings of the International Symposium on Water Management and Hydraulic Engineering*, Ohrid, Macedonia, 137–148.

Hungr, O. & Jakob, M. (2005), *Debris-Flow Hazards and Related Phenomena*, Springer, Berlin.

Hutter, K., Svendsen, B. & Rickenmann, D. (1996), Debris flow modeling: a review, *Continuum Mechanics and Thermodynamics*, **8**, 1–35.

Iverson, R. M. (1997), The physics of debris flows, *Review of Geophysics*, **35**(3), 245–96.

Iverson, R. M. (2003), The debris-flow rheology myth, in C. Chen and D. Rickenmann (eds.), *Debris Flow Mechanics and Mitigation Conference*, Mills, Davos, 303–14.

Kaitna, R., Rickenmann, D. & Schatzmann, M. (2007), Experimental study on rheologic behaviour of debris flow material, *Acta Geotechnica*, **2**(2), 71–85.

Kowalski, J. (2008), Two-phase modeling of debris flow, Ph.D. thesis, ETH Zurich.

Kowalski, J. & McElwaine, J. N. (2013), Shallow two-component gravity-driven flows with vertical variation, *Journal of Fluid Mechanics*, **714**, 434–62.

Leonardi, A., Wittel, F. K., Mendoza, M. & Herrmann, H. J. (2013), Multiphase debris flow simulations with the discrete element method coupled with a Lattice-Boltzmann fluid, in M. Bischoff, E. Ramm, M. Oñate, R. Owen, and P. Wriggers (eds.), *III International Conference on Particle-Based Methods – Fundamentals and Applications*, Stuttgart, 276–87.

Leonardi, A., Wittel, F. K., Mendoza, M. & Herrmann, H. J. (2014a), Coupled DEM-LBM method for the free-surface simulation of heterogeneous suspensions, *Computational Particle Mechanics*, **1**, 3–13.

Leonardi, A., Wittel, F. K., Mendoza, M. & Herrmann, H. J. (2014b), Lattice-Boltzmann method for geophysical plastic flows, in W. Wu (ed.), *Recent Advances in Modeling Landslides and Debris Flows*, Springer International Publishing, Switzerland, pp. 131–40.

Moriguchi, S., Borja, R. I., Yashima, A. & Sawada, K. (2009), Estimating the impact force generated by granular flow on a rigid obstruction, *Acta Geotechnica*, **4**(1), 57–71.

Newmark, N. M. (1959), A method of computation for structural dynamics, *Journal of the Engineering Mechanics Division*, **85**(EM 3), 67–94.

Owen, D. R. J., Leonardi, C. R. & Feng, Y. T. (2011), An efficient framework for fluid–structure interaction using the lattice Boltzmann method and immersed moving boundaries, *International Journal for Numerical Methods in Engineering*, **87**, 66–95.

Pöschel, T. & Schwager, T. (2005), *Computational Granular Dynamics*, Springer, Berlin.

Scheidl, C., Chiari, M., Kaitna, R., Müllegger, M., Krawtschuk, A., Zimmermann, T. & Proske, D. (2012), Analysing debris-flow impact models, based on a small scale modelling approach, *Surveys in Geophysics*, **34**(1), 121–40.

Sun, W., Kuhn, M. R. & Rudnicki, J. W. (2013), A multi-scale DEM-LBM analysis on permeability evolutions inside a dilatant shear band, *Acta Geotechnica*, **8**(5), 465–80.

Švec, O., Skoček, J., Stang, H., Geiker, M. R. & Roussel, N. (2012), Free surface flow of a suspension of rigid particles in a non-Newtonian fluid: a lattice Boltzmann approach, *Journal of Non-Newtonian Fluid Mechanics*, **179–180**, 32–42.

Takahashi, T. (2007), *Debris Flow, Mechanics, Prediction and Countermeasures*, Taylor & Francis, London.

Teufelsbauer, H., Wang, Y., Chiou, M. C. & Wu, W. (2009), Flow–obstacle interaction in rapid granular avalanches: DEM simulation and comparison with experiment, *Granular Matter*, **11**(4), 209–20.

Teufelsbauer, H., Wang, Y., Pudasaini, S. P., Borja, R. I. & Wu, W. (2011), DEM simulation of impact force exerted by granular flow on rigid structures, *Acta Geotechnica*, **6**(3), 119–33.

vander Heijden, A. M. (2008), ed. *W.T. Koiter's Elastic Stability of Solids and Structures*, Cambridge University Press, Cambridge.

vanWesten, C., vanAsch, T. & Soeters, R. (2005), Landslide hazard and risk zonation—why is it still so difficult? *Bulletin of Engineering Geology and the Environment*, **65**(2), 167–84.

vonBoetticher, A., Glover, J., Volkwein, A. & Denk, M. (2011), Modelling flexible wire netting applied to rock fall attenuating systems, in *Proceedings of Interdisciplinary Workshop on Rockfall Protection*, Innsbruck, 71–72.

vonBoetticher, A. G. (2013), Flexible Hangmurenbarrieren: eine numerische Modellierung des Tragwerks, der Hangmure und der Fluid-Struktur-Interaktion, Ph.D. thesis, Technische Universität München.

Vetter, R., Stoop, N., Jenni, T., Wittel, F. K. & Herrmann, H. J. (2013), Subdivision shell elements with anisotropic growth, *International Journal for Numerical Methods in Engineering*, **95**, 791–810.

Volkwein, A., Roth, A., Gerber, W. & Vogel, A. (2009), Flexible rockfall barriers subjected to extreme loads, *Structural Engineering International*, **3**, 327–32.

Volkwein, A., Wendeler, C., Mcardell, B. & Roth, A. (2006), Mitigation of debris flow hazard by means of flexible barriers, in *Proceedings of International Disaster Reduction Conference*, Davos, Switzerland, 616–18.

Wendeler, C. (2008), Murgangrückhalt in Wildbächen - Grundlagen zu Planung und Berechnung von flexiblen Barrieren, Ph.D. thesis, ETH Zurich.

Wendeler, C., Haller, B. & Salzmann, H. (2012), Protection against debris flows with 13 flexible barriers in the Milibach River (Canton Berne, Switzerland) and first event analysis, in C. Lau, E. Chan, and J. Kwan (eds.), *Proceedings of the One Day Seminar on Natural Terrain Hazards Mitigation Measures*, Hong Kong, The Association of Geotechnical and Geoenvironmental Specialists (Hong Kong) Limited, 22–28.